Laser-induced transient currents in CdZnTe quasi-hemispherical radiation detector

R. Grill[1] (grill@karlov.mff.cuni.cz), M. Betušiak[1], M. Bettelli[2], P. Praus[1], L. Abbene[3], J. Pipek[1], E. Belas[1], A. Zappettini[2]

[1]Charles University, Faculty of Mathematics and Physics, Institute of Physics, Ke Karlovu 5, Prague 2, CZ–121 16, Czech Republic

[2]IMEM-CNR, Parco Area Delle Scienze 37A, 43124 Parma, Italy

[3]Department of Physics and Chemistry (DiFC)-Emilio Segrè, University of Palermo, 90128 Palermo, Italy

Abstract

Laser-induced transient currents were measured after applying pulsed or direct-current bias to a CdZnTe quasi-hemispherical radiation detector with gold contacts. The temporal evolution of current transients was analyzed to evaluate the dynamics of the space charge formation and its spatial distribution. The observed effects were explained by a model involving hole injection from positively biased contacts. Experimental results were complemented by numerical simulations, which supported the model. This paper discusses how the detected phenomena affect the detector performance and proposes an improved detector design.

Quasi-hemispherical-electrode CdZnTe radiation detectors are convenient to mitigate the poor hole collection that normally degrades detector performance with this material [1]. Unlike other geometries, the quasi-hemispherical detector [2], [3] allows charge collection over large detector volumes (up to 4 cm^3) [4] with a single readout channel. Furthermore, the fabrication procedure produces no critical points because all electrodes are deposited in a single step after photolithography. In addition, quasi-hemispherical detectors do not require pulse-shape analysis [4]—their state-of-the-art performance stems simply from the raw spectrum. The easy readout, large volume, and high performance make these detectors appealing in several applications, such as environmental monitoring, radioisotope identification [5], gamma-neutron detection [6], and nuclear physics [7].

The asymmetric electrode formed by an extensive cathode and a pixel-type anode produces a strongly divergent electric field, accelerating charge near the anode and slowing charge near the cathode. The region near the pixel dominates the charge-collection efficiency, which is further boosted by the weighting-field distribution and which accentuates the current near the pixel [1]. Consequently, the collected charge comes mainly from electrons collected at positively biased pixel while the hole contribution is damped. Although the sensing characteristics of the (quasi-)hemispherical detector have been studied experimentally and theoretically [8], no detailed analysis yet exists of the charge transport in the detector, the space charge (SC) formation, and the polarization induced by specific contact designs.

To address this situation, this paper reports our investigation of the transient currents in a CdZnTe detector with cuboidal dimensions 4.2 × 4.2 × 3 mm^3 grown using the travelling heater method developed by Redlen Technologies (Canada) [9]. The crystals were processed following the standard procedure developed at IMEM-CNR (Parma, Italy) and equipped with gold electroless contacts deposited from methanol solution [10]. Details of the sensor preparation are available in the supplementary materials (SM). A 0.2-mm-diameter pixel

(anode) and a 0.5-mm-wide guard electrode (GE) were fabricated in the center and on the periphery, respectively, of a larger side. A full electrode (FE) biased as the cathode was deposited on the opposite side. Figure 1 shows the detector layout with contacts. Reference [4] provides a photograph of another detector prepared at IMEM-CNR. As opposed to the standard quasi-hemispherical geometry where the cathode completely covers five faces of the detector, the GE allows the sample to be wired in (i) the quasi-hemispherical (Q-hemi) configuration, where the GE is maintained at the same potential as the FE, or in (ii) the quasi-planar (Q-pln) configuration, where the GE is connected to the pixel. The specific contact design allows us to gather additional experimental data to better comprehend processes occurring in the biased detector, thereby refining the theoretical model. Figure S1 of the SM presents the direct-current *I-V* characteristics. In the Q-hemi configuration, the electric current reaches 2 nA at 400 V.

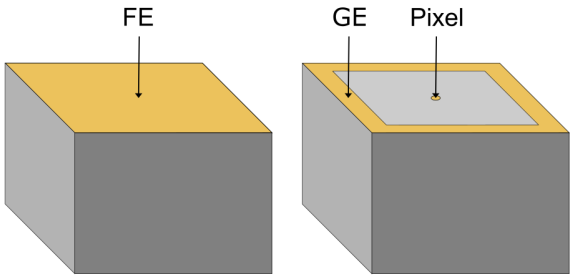

Figure 1: Detector layout of the planar cathode (left) and the anode pixel and guard electrode (right).

The SC distribution within the sample is investigated by applying the laser-induced transient-current technique. Details of the setup are available elsewhere [11], [12], [13]. For this paper, we applied a bias voltage of 50–400 V and used 670 nm laser pulses (≈500 ps) to photoexcite above the band gap. The laser pulse intensity was sufficiently low to suppress electron-hole plasma screening effects and internal Coulomb repulsion in the drifting charge cloud. By controlling the laser pulse delay after applying the bias voltage and analyzing the current waveforms (CWFs), we derived the electric-field profile along the trajectory of the charge drift and determined the corresponding SC distribution. Figure S2 of the SM shows a detailed timing scheme for the bias and laser pulses.

Current transients were numerically simulated in three dimensions based on the geometry of the detector and the experimental apparatus. Comsol Multiphysics software was used to calculate the electric and weighting fields. The drift velocity and weighting field along the electric-field lines were used to determine the electron current waveforms, which were subsequently integrated over the illuminated area and weighted with a Gaussian beam profile. The SC formation was modeled by using a one-dimensional (1D) model based on the drift-diffusion and Poisson equations. The model, discussion, and principal results are presented below. Auxiliary information, secondary results, and a table of acronyms are supplied in the SM, whose figures are prefixed by "S".

Figure 2 shows electron CWFs measured 100 µs after applying the bias with the detector in the Q-hemi and Q-pln configurations. The curves are plotted against the product of time and bias (Time × Bias). The CWFs measured in the Q-hemi configuration [Fig. 2(a)]

conform to the theoretical prediction [1]; they go through a significant peak in their terminal part, which corresponds to charge drift near the pixel (i.e., with the large electric and weighting fields oriented in parallel to enhance the CWF). The CWFs measured in the Q-pln configuration [Fig. 2(b)] reveal charge drift in addition to the terminal peak. It manifests as the flat part of CWFs and corresponds to charge collection at the positively biased GE. The CWFs plotted in Figs. 2(a) and 2(b) are consistent with the detector geometry, which is supported by numerical simulation (see Figs. S3 and S4).

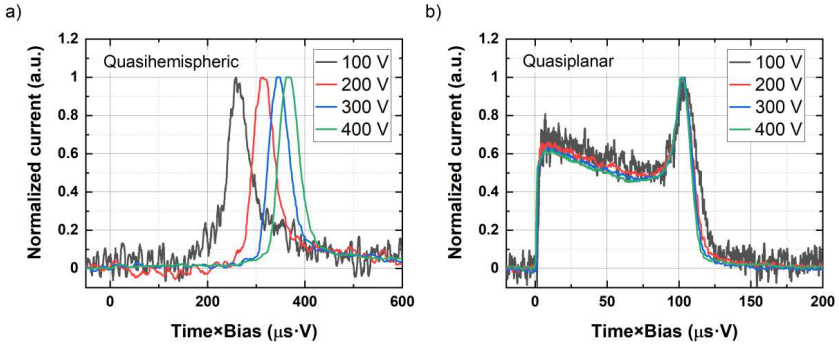

Figure 2: Electron current waveforms measured in (a) quasi-hemispheric and (b) quasi-planar configurations by using pulsed bias and measuring the current waveforms after 100 μs. The current is normalized to the maximum value.

Measurements made immediately after biasing are vital because they monitor the state of a nonpolarized sample (i.e., the sample without bias-induced SC). In this case, the electric field $\boldsymbol{E}(\boldsymbol{r})$ and drift velocity $\boldsymbol{v}(\boldsymbol{r})$ are linearly proportional to the applied bias U and weighting field $\boldsymbol{E}_w(\boldsymbol{r})$: $\boldsymbol{E}(\boldsymbol{r}) = U\boldsymbol{E}_w(\boldsymbol{r})$ and $\boldsymbol{v}(\boldsymbol{r}) = \mu_e U\boldsymbol{E}_w(\boldsymbol{r})$, where the electron drift mobility μ_e is constant at the low electric fields used in these experiments. Plotting CWFs versus time × bias is particularly useful for demonstrating the linear scaling of the transit time, which is the time required for carriers to pass through the detector for a given applied bias. The dependence of the CWF on time × bias also enables a visual comparison of CWFs measured over a wide range of biases. Considering that the electron lifetime is much greater than the transit time (this is common in today's high-quality detectors), the CWF shapes should be independent of bias, except for the weak diffusion broadening at low bias. CWFs measured in the Q-pln configuration [Fig 2(b)] are entirely consistent with the predicted behavior. These CWFs were used for evaluating the electron drift mobility in this material, which is μ_e= 1050 cm^2 V^{-1} s^{-1}. In contrast, CWFs measured in the Q-hemi configuration [Fig. 2(a)] deviate considerably from the theory, revealing a remarkable increase in transit time with increasing bias. Moreover, the measured electron transit time τ_{tr} is much shorter than predicted by numerical simulations. For example, theory predicts τ_{tr} = 2.9 μs for Q-hemi detection at 400 V bias [see Fig. S4(a)], whereas experiment yields τ_{tr} = 0.9 μs. These anomalies are considered in developing our model.

Next, we explore the temporal evolution of CWFs in the biased detector. Since the geometry and weighting field of the sample are fixed, any changes can only be due to SC. Detailed monitoring of the CWF can thus supply unique information on the SC dynamics. Figures 3(a) and 3(b) show the temporal evolution of CWFs of the sample biased at 400 V and measured in the Q-hemi and Q-pln configurations, respectively. In both cases, the CWFs change gradually. The Q-hemi CWFs reveal a reduction in τ_{tr}, which may be interpreted as a positive charging of the detector interior. This enhances the electric field near the cathode and

compensates for the low electric field caused by the quasi-hemispherical geometry. This conclusion is supported by the increase in charge collected due to less surface recombination of carriers excited near the cathode, which results from the enhanced electric field at the metal-semiconductor interface.

The evolution of the Q-pln CWFs in Fig. 3(b) is more complex. Several features must be addressed: (i) the rapidly decaying peak representing charge collection at the pixel, which nearly disappears in the initial 20 ms of biasing; (ii) the partial recovery of this peak after 1 s; (iii) the significant increase in the initial current over the first 20 ms after biasing; and (iv) the subsequent descent and stabilization of the shoulder (its DC shape is similar the shape shortly after biasing).

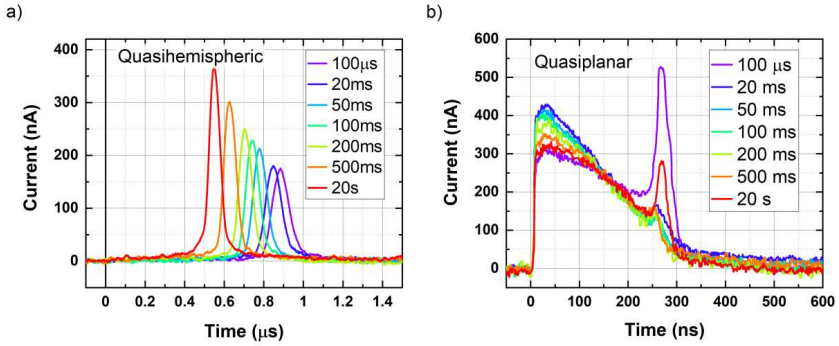

Figure 3: Temporal evolution of CWFs of sample biased at 400 V measured in (a) quasi-hemispheric and (b) quasi-planar configurationffs.

The following model for SC buildup is proposed to explain the experimental data presented in Figs. 2 and 3. The cornerstone of the model is the hypothesis that all effects are incited by strong hole injection from positively biased contacts (i.e., the pixel in the Q-hemi and the pixel plus the GE in the Q-pln configurations). Electrons are not considered in this model of SC formation, and the positive SC potentially formed by the blocking cathode cannot be distinguished experimentally. For the Q-hemi configuration, charge injection is so fast that a significant SC is created near the pixel already in the initial 100 μs. For this reason, the CWFs in Fig. 2(a) deviate from the predicted bias-independent shapes and τ_{tr} is much shorter than expected [see Fig. S4(a)]. The continuation of the process further amplifies the SC and progressively shortens τ_{tr}, as is apparent in Fig. 3(a). In the case of low bias, the ongoing polarization and shortening of τ_{tr} are less evident. Even at biases lower than 120 V, τ_{tr} is extended.

For the Q-pln configuration, the positive charging is dominated by hole injection from the GE, which has a much larger area than the pixel. The positive charge spreads from the GE mainly along the sides of the detector and penetrates through the detector bulk, inducing lateral divergence of field lines toward the GE. Subsequently, drifting electrons deflect to the GE and the charge collected at the pixel diminishes so that the respective maximum in Fig. 3(b) dampens in agreement with item (i) above. The strong damping of the pixel peak may be also amplified by a lateral tilt of the electric field induced by possible nonsymmetrical charging of the sample. The formation of positive SC near the cathode enhances the transient current when the CWF shoulder begins to grow in concert with item (iii). Figure S4(b) shows the respective simulation.

The characteristic property of SC arising from the injecting contact is its bulk damping, far from the contact, which is caused by the screening of the electric field by the SC formed near contact and the subsequent reduction in charge injection. The SC then becomes localized near the contact and decreases throughout the rest of the sample. Figure S5 demonstrates this effect by showing a numerical simulation of the electric field and CWF evolution using a 1D model of a planar sample. This simulation is based on the coupled drift-diffusion and Poisson equations and considers a strongly injecting anode and a hole trap. The disappearance of SC in the detector bulk far from the anode leads to partial recovery of the pixel signal defined in item (ii) and of the shoulder representing the charge collected from the GE, in agreement with item (iv).

To verify and strengthen the proposed model, another set of experiments was carried out in which the structure and formation of SC near the pixel in the Q-hemi configuration were investigated in detail. The experiment was designed to determine whether the SC is distributed in the bulk beneath the pixel or at the surface around the pixel. We thus illuminated and probed the pixel side and measured the transient hole current. The laser spot was slightly larger than the pixel. Despite the generally bad hole collection in CdZnTe, the large electric and weighting fields near the pixel allowed the hole signal to be detected with sufficient signal-to-noise ratio to evaluate the collected charge. Transients were measured not only during SC formation but also after the bias was switched off, at which point the decaying residual electric field was controlled by SC dissipation. Figure 4(a) shows the results of the experiment. The collected charge is normalized to the value obtained 100 μs after the onset of biasing.

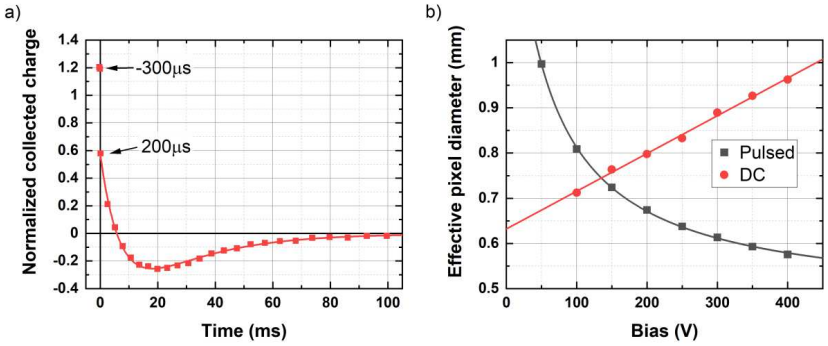

Figure 4: (a) Collected charge plotted as a function of time after biasing. The charge is derived from transient currents measured at a specific times after switching off the 400 V bias at time zero. The first point labeled −300 μs was measured 300 μs before switching off the bias. The sample was biased for 50 ms. (b) Effective pixel diameter plotted as a function of bias. The pixel diameter was derived from the shortening of the transit time of the CWFs in Fig. 2(a) at different biases. The value for DC CWF at 50 V bias could not be determined due to noise at long τ_{tr}.

Initially, the collected charge increases by 20% during the 50-ms-long biasing period. This feature is explained by an extension of hole lifetime τ_h induced by the filling of hole traps during the formation of a positive SC around the pixel. The most prominent effect appears after switching off the bias. The signal remains positive up to ≈8 ms during the discharge period, which testifies to a persisting positive electric field near the surface around the pixel. This result, combined with the known positive SC in the bulk, indicates that a positive SC must exist at the surface to deflect the electric field into the bulk. After switching off the bias, the dominance of the positive surface charge vanishes with a characteristic time of 10 ms and the

collected charge i.e., the electric field around the pixel changes the sign. This effect indicates that positive SC is distributed in the bulk in this period. The bulk SC attenuates with a characteristic time estimated to be 25 ms.

The dominance of the surface SC over the bulk SC and the fast evolution of the former indicates that the fast formation of surface SC is the main factor that shortens τ_{tr} in the Q-hemi configuration. This in turn causes the loss of the linear scaling of the CWFs with bias seen in Fig. 2(a). No analogous effect is detected in the Q-pln configuration, where the lateral component of the electric field oriented from the pixel along the detector surface is small.

This hypothesis allows us to evaluate the properties of the surface SC formed in the Q-hemi configuration during the initial 100 μs after biasing. Since the defect structure and exact SC distribution are unknown, SC formation is described by enlarging a real pixel diameter d to an effective diameter d_{eff} that fits the experimentally determined τ_{tr}. Figure 4(b) plots in black the respective d_{eff}. The calculated d_{eff} is the minimum value required to fit τ_{tr}, assuming that the charge density on the metal contact is the same as that on the free detector surface. However, in reality, the charge density at the free surface is less, so d_{eff} is larger. A precise determination of d_{eff} would need to specify model details, namely the structure of the surface defect states, which are out of the scope of this paper.

The ongoing polarization shown in Fig. 3(a) proceeds at a much slower rate and stabilizes within seconds. Polarization in both the Q-hemi and Q-pln configurations evolves similarly, which evinces that the polarization caused by the bulk SC formation is induced by the hole injection. Figure 4(b) (in red) characterizes τ_{tr} and SC through d_{eff} measured in DC bias mode. A surprising phenomenon appears whereby the polarization at large bias proceeds further and d_{eff} increases, whereas d_{eff} at low bias (<120 V) has the opposite behavior and d_{eff} decreases. We attribute this feature to screening of the electric field at the pixel by the bulk SC. At low bias, the bulk SC is localized in proximity to the pixel, about 37 μm at 50 V in contrast to 150 μm at 400 V, as calculated with the 1D defect model of the SM. Nevertheless, a detailed comprehension of this effect requires further investigation.

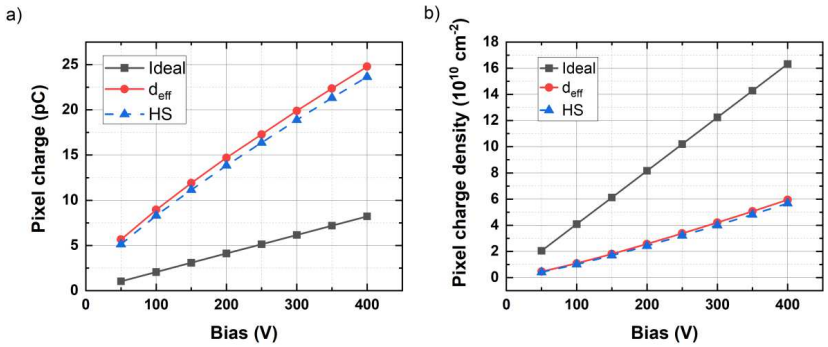

Figure 5: (a) Pixel charge immediately after biasing calculated numerically (black) and effective pixel charge derived from transit time measured 100 μs after biasing (red). (b) Charge density in the real pixel (black) and in the effective pixel (red) corresponding to charges from panel (a). The blue dashed lines show the effective pixel charge and respective pixel charge density calculated analytically.

Describing SC by means of d_{eff} enables us to estimate the characteristics of SC distributed at the surface. Figure 5(a) shows the calculated charge on the pixel immediately after biasing (i.e., in the ideal nonpolarized detector) and with the charge corresponding to d_{eff}

100 μs after biasing. Figure 5(b) shows the charge density in the real pixel and in the effective pixel. The rather large surface SC density of the order 10^{10} e/cm^2 seems realistic in comparison with other works that report densities as large as 10^{13} e/cm^2 measured in nitrogen-doped p-CdTe by the deep-level transient spectroscopy [14]. The solid curves plotted in Fig. 5 were calculated numerically by considering the exact quasi-hemispherical detector geometry. The procedure may be simplified by using an analytical formula relating the effective pixel diameter and the effective pixel charge Q_{eff}: $Q/d \approx Q_{\text{eff}}/d_{\text{eff}}$, which is valid for the Q-hemi configuration for pixel sizes much less than the sample dimension [1]. Respective curves are plotted by blue dashed lines in Fig. 5. This simple formula fits the charge satisfactorily, with the numerical results deviating less than 10%.

Summarizing, the charge collection in the investigated quasi-hemispherical detector proceeds much faster than predicted by theory. This feature is explained by the positive SC appearing near the pixel anode due to the hole injection. The surface SC arises less than 100 μs after biasing, moving into the bulk on the scale of seconds. The SC has a double effect: it increases the electric field in the detector bulk (which improves charge collection), and it reduces the electric field near the anode and captures drifting electrons in the SC region (which leads to incomplete charge collection). As a result, there exists a pixel size that optimizes charge collection and spectroscopic performance. In fact, as shown by Vicini *et al.* [4], a quasi-hemispherical detector with small pixels (250 μm) performs much worse than the same detector with larger pixels (750–1500 μm). The development of contacts able to suppress hole injection from the positively biased pixel is thus recommended to better stabilize quasi-hemispherical detectors.

Supplementary Material

This file describes the sensor's preparation, the current-voltage characteristics, the bias and laser-pulse timing schemes, the numerical simulation of the electric field lines and of the CWFs in the real geometry, and the numerical simulation of SC formation in the 1D approximation. A list of acronyms and symbols is also provided.

This work was financially supported by the Grant Agency of the Czech Republic under Grant No. P102-19/11920S and the Grant Agency of Charles University under Grant No. 393222 and Charles University Grant No. SVV–2023–260720.

References:

[1] H.L. Malm, D. Litchinsky, C. Canali, "Single carrier charge collection in semiconductor nuclear detectors," Revue de Physique Appliquee **12**(2), 303 (1977).
doi: 10.1051/rphysap:01977001202030300

[2] C. Szeles, D. Bale, J. Grosholz, Jr., G.L. Smith, M. Blostein, J. Eger, "Fabrication of high-performance CdZnTe quasi-hemispherical gamma-ray CAPture plus detectors," Proc. SPIE 6319, Hard X-Ray and Gamma-Ray Detector Physics and Penetrating Radiation Systems VIII, 631909 (2006);
https://doi.org/10.1117/12.683552

[3] A. Loutchanski, V. Fjodorovs, V. Ivanov, & V. Ogorodniks, "Application of CdZnTe quasi-hemispherical detectors in strong gamma radiation fields," EPJ Web Conf. **225**, 07004 (2020).
doi.org/10.1051/epjconf/202022507004

[4] V. Vicini, S. Zanettini, N. Sarzi Amadè, R. Grill, N. Zambelli, D. Calestani, A. Zappettini, L. Abbene & M. Bettelli, "Optimization of quasi-hemispherical CdZnTe detectors by means of first principles simulation," Scientific Reports **13**, 3212 (2023).
doi.org/10.1038/s41598-023-30181-2

[5] Y. Wang, C. Feng, M. Zhao, C. Shan, F. Liu, Q. Lei, Z. Zhou, S. Liu, "Development of a high energy resolution and wide dose rate range portable gamma-ray spectrometer," Applied Radiation and Isotopes **192**, 110572 (2023).
doi.org/10.1016/j.apradiso.2022.110572

[6] L. Bao, G. Zha, J. Li, L. Guo, J. Dong & W. Jie, "CdZnTe quasi-hemispherical detector for gamma–neutron detection," Journal of Nuclear Science and Technology **56**(5), 454 (2019).
doi: 10.1080/00223131.2019.159272

[7] L. Abbene, M. Bettelli, A. Buttacavoli, F. Principato, A. Zappettini et al. New opportunities for kaonic atoms measurements from CdZnTe detectors,". The European Physical Journal Special Topics (2023).
doi.org/10.1140/epjs/s11734-023-00881-x

[8] D.S. Bale & C. Szeles, "Design of high-performance CdZnTe quasi-hemispherical gamma-ray CAPture plus detectors," Proc. SPIE 6319, Hard X-Ray and Gamma-Ray Detector Physics and Penetrating Radiation Systems VIII, 63190B (2006).
https://doi.org/10.1117/12.683702

[9] H. Chen, S.A. Awadalla, J. Mackenzie, R. Redden, G. Bindley, A.E. Bolotnikov, G.S. Camarda, G. Carini, R.B. James, "Characterization of Traveling Heater Method (THM) Grown $Cd_{0.9}Zn_{0.1}Te$ Crystals," IEEE Trans. Nucl. Sci. **54**(4), 811 (2007).
doi: 10.1109/TNS.2007.902369.

[10] G. Benassi, L. Nasi, M. Bettelli, N. Zambelli, D. Calestani and A. Zappettini, "Strong mechanical adhesion of gold electroless contacts on CdZnTe deposited by alcoholic solutions," Journal of Instrumentation **12**, P02018 (2017).
doi:10.1088/1748-0221/12/02/P02018

[11] K. Suzuki, T. Sawada, and K. Imai, "Effect of DC Bias Field on the Time-of-Flight Current Waveforms of CdTe and CdZnTe Detectors," IEEE Transactions on Nuclear Science **58**(4), 1958 (2011).
doi: 10.1109/TNS.2011.2138719.

[12] E. Belas, R. Grill, J. Pipek, P. Praus, J. Bok, A. Musiienko, P. Moravec, O. Tolbanov, A. Tyazhev, and A. Zarubin, "Space charge formation in chromium compensated GaAs radiation detectors," Journal of Physics D: Applied Physics **53**(47), 475102 (2020).
doi: 10.1088/1361-6463/aba570.

[13] J. Pipek, M. Betušiak, E. Belas, R. Grill, P. Praus, A. Musiienko, J. Pekarek, U.N. Roy, and R.B. James, "Charge Transport and Space-Charge Formation in $Cd_{1-x}Zn_xTe_{1-y}Se_y$ Radiation Detectors," Physical Review Applied **15**(5), 054058 (2021). doi: 10.1103/PhysRevApplied.15.054058.

[14] K. Wichrowska, T. Wosinski, Z. Tkaczyk, V. Kolkovsky, and G. Karczewski, "Surface acceptor states in MBE-grown CdTe layers," Journal of Applied Physics **123**, 161522 (2018). doi.org/10.1063/1.4986157